Check for updates

Original Research

Advances in Structural Engineering

Aftershock Fragility Assessment of Steel Gabled Frames Consisting of Web-Tapered Members

Advances in Structural Engineering
2023, Vol. 0(0) 1–19
© The Author(s) 2023
Article reuse guidelines:
sagepub.com/journals-permissions
DOI: 10.1177/13694332221148546
journals.sagepub.com/home/ase
SAGE

Mohammad Malekizadeh[1], Nader Fanaie[2] and Ali A Pirasteh[3]

Abstract

Due to the widespread construction of steel gabled frame systems throughout the world, many of them are located in regions with high seismicity and experience sequential strong events in the future. Previous studies have clearly shown that the damage caused by the mainshock modifies the overall strength and stiffness and consequently dynamic response to the aftershock. However, the current structural design process only considers the main seismic event, and the post-mainshock scenarios and their effects are generally ignored. In order to address this issue, in the present study, the mainshock incremental dynamic analysis (IDA) was first conducted on four SGFs. Then mainshock damage states based on the transient absolute maximum drift angle were considered, and aftershock incremental dynamic analysis analysis was performed on the mainshock-damaged structures. Aftershock fragility curves using probabilistic seismic demand models for transient absolute maximum drift angle and median IDA curves for residual absolute maximum drift angle were developed to compare intact and pre-damaged SGFs. The results showed that aftershocks significantly increase the vulnerability of short-period SGFs when higher damages are induced during mainshock, where the aftershock collapse capacity is reduced by up to 13% for the largest mainshock damage state. It was also found that in terms of aftershock collapse capacity associated with the residual absolute maximum drift angle, long-period SGFs require major realignment while short-period SGFs cannot be repaired.

Keywords

Steel gabled frames, seismic sequences, aftershock IDA analysis, aftershock PSDMs, aftershock fragility curves

Introduction

A very common form of construction in low-rise non-residential structures is the steel gabled frame (SGF) system. SGFs account for approximately 50% of the total low-rise non-residential construction market in the United States (MBMA 2012). They are affordable and durable and provide fast construction planning. Also, they are easy to expand and fully customizable for an owner's needs. SGFs are used for a wide range of applications including warehouses, sports complexes, conference halls, aircraft hangars, industrial factories, pools, churches, storage and many others. SGFs are usually built from single-story steel moment frames in their transverse direction. They are typically made with built-up I section, often with tapered webs, which have been optimized to minimize material weight (Newman 2004).

SGFs are built in a variety of locations, including regions with high seismicity. Hence, they are likely to experience sequential strong events in the future. However, the current structural design process only considers the main seismic event, and the post-mainshock scenarios and their effects are generally ignored. Damage due to the mainshock modifies the overall strength and stiffness and consequently dynamic response to the aftershock (Nazari et al., 2015). On the other hand, aftershocks usually have different duration, amplitude, frequency and energy content compared to the mainshock (Alliard and Léger 2008;

[1]Department of Civil Engineering, Academic Center for Education, Culture and Research, Ahvaz, Iran
[2]Department of Civil Engineering, K. N. Toosi University of Technology, Tehran, Iran
[3]Department of Civil Engineering, Faculty of Engineering, Shahid Chamran University of Ahvaz, Ahvaz, Iran

Corresponding author:
Nader Fanaie, Civil Engineering Department, K. N. Toosi University of Technology, No. 1346, Vali-Asr Street, P.O. Box. 15875-4416, Tehran 19697, Iran.
Email: fanaie@kntu.ac.ir

Song et al., 2013). Therefore, when an aftershock occurs, a different structure with lower resistance and stiffness encounters a new earthquake with different frequency content, and consequently, different seismic performances may be required.

Aftershocks occur in the following hours, months, or even years with different characteristics compared to the corresponding mainshock. For example, in Gorkha, Nepal on 25 April 2015, an earthquake with a magnitude of 7.8 was followed by several aftershocks, including a magnitude 7.3 event on May 12, 2015 (Feng et al., 2017). Similar seismic sequences were observed during the Wenchuan (China, 2008), Tohoku (Japan, 2011) and Amatrice (Italy, 2016) earthquakes, which the aftershocks caused additional damage to mainshock-damaged structures (Huang et al., 2008; Hirose et al., 2011; Michele et al., 2016). Hence, in recent years, there has been a growing interest in the performance evaluation of structures subjected to seismic sequences. These studies investigated the impact of seismic sequences on various types of structures, such as conventional frames (Khansefid 2021a; Ghasemi et al., 2021; Moustafa and Takewaki 2016; Trevlopoulos et al., 2020), structures equipped with vibration control systems (Han et al., 2014; Rinaldin et al., 2017; Khansefid 2021b; Zhai et al., 2017), dams (Wang et al., 2017; Zhang et al., 2013), bridges (Chen et al., 2022; Ge et al., 2012), nuclear structure (Wang et al., 2019) and reticulated dome (Zhang et al., 2020). In addition, new studies were conducted using self-centering techniques to improve the seismic performance of structures under seismic sequences (Silwal and Ozbulut 2018; Shi et al., 2020). However, seismic sequences inclusion in studies on the seismic performance of SGFs is rare.

To evaluate the seismic performance of structures under seismic sequences, different performance indicators were used to specify damage caused by the mainshock. Most studies employed damage states associated with transient maximum drift angle to define post-mainshock damage states (Han et al., 2015; Raghunandan et al., 2015; Song et al., 2014). The importance of residual drift angles in seismic design was discussed by Pristley (1993) but has recently been considered as a significant measure for evaluating the seismic performance of structures (Amiri and Bojórquez 2019; Ruiz-García and Miranda 2006a, 2010). FEMA P-58 (2000) recommendations use residual drift angles to determine the post-mainshock condition of structures and the economic feasibility of repairing them. Ruiz-Garcia and Miranda (2006b) and Ruiz-Garcia and Aguilar (2015) suggested the use of residual drift angle as a damage indicator to predict the seismic performance of steel frame buildings under seismic sequences. They showed that residual maximum drift angle, which can be measured during structural analyses after a seismic event, compared to transient maximum drift angle, can be a better parameter to define post-mainshock damage states during evaluating the seismic performance under aftershocks.

The shaking table tests on the seismic behavior of SGFs consisting of web-tapered members were also performed by several researchers (Hong and Uang, 2012; Wang et al., 2012; Su et al., 2017, 2018, 2021a). The experimental results showed that these systems had high deformability, but the ductility was limited. Also, Malekizadeh et al. (2017, 2018; 2021a) showed in their analytical studies that with the increase of the span of SGFs, the effect of the earthquake load becomes significant and it is necessary to evaluate their seismic performance carefully. Previous studies on SGFs were analysed assuming the mainshock only and the effects of aftershocks were ignored. Therefore, despite the widespread construction of SGF systems throughout the world, there is a lack of knowledge regarding their seismic performance under seismic sequences. Also, despite the conventional residential buildings, SGFs under seismic sequences have their own specific seismic performance that should be studied. In order to address this issue, the continuation of the present article is organized as follows. In Section 2, details of the studied SGFs in terms of geometric characteristics and nonlinear modeling are presented. The characteristics of ground motion sequences consistent with the site are presented in Section 3. In Section 4, mainshock incremental dynamic analysis (IDA) is conducted on four SGFs. In Section 5, mainshock damage states based on the transient absolute maximum drift angle are considered and aftershock IDA analysis is performed for the mainshock-damaged structures. At the end of the 4th and 5th sections, the efficiency-sufficiency test of the intensity measure (IM) related to the mainshock and the aftershock is presented. In Section 6, aftershock fragility curves using probabilistic seismic demand models (PSDMs) for transient absolute maximum drift angle and median IDA curves for residual absolute maximum drift angle are developed to compare intact and pre-damaged SGFs. Finally, the seismic performance of the studied SGFs subjected to seismic sequences is evaluated. The results are discussed at different mainshock damage states, and some concluding remarks on the seismic performance of SGFs subjected to seismic sequences are presented in Section 7.

SGF geometry and nonlinear modeling

In the present study, four 2D SGF models with different spans and heights were extracted from the research conducted by Malekizadeh et al. (2021b, 2022a, 2022b). The span width of models A, B, C and D were 20, 20, 60 and 60 m, respectively, and their column heights were 6, 12, 6 and 12 m, respectively. The geometry of the SGF model is revealed in Figure 1(a). As shown in Figure 1(a), the all length of the columns as well as the area with a length of

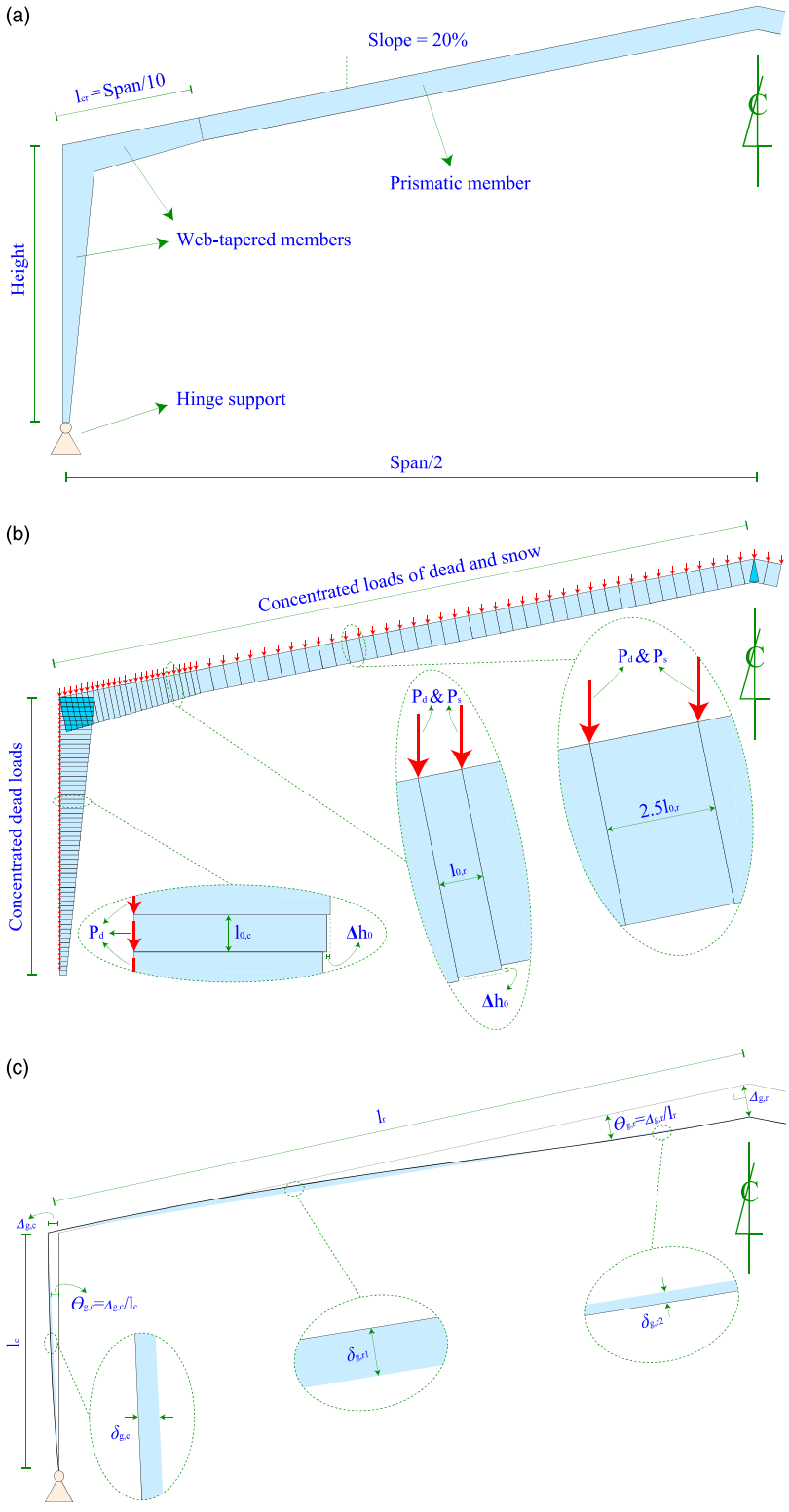

Figure 1. (a) SGF model geometry, (b) SGF model developed in OpenSees and (c) deformations created in the SGF model under gravity loads.

span/10 in rafters from the eave line (l_{cr}) are assigned by web-tapered members, while the remainder of the length of the rafters up to the ridge is prismatic. The roof slope was 20% and the support of the columns was hinge. Table 1 declares the section dimensions of the rafter and column members. The used steel was of ST37 type with the elasticity modulus of 2.039 E + 10 kgf/m^2. In all SGF models, ordinary moment frame (OMF) was used as the lateral force-resisting system. The models were also located in an area with high seismicity with tectonic characteristics of Class D soil in accordance with NEHRP (2000). More details about the design of structures can be found in the studies of Malekizadeh et al. (2021b, 2022a, 2022b).

OpenSees software (2018) was used as open source software for nonlinear modeling and SGF model analysis. Rayleigh damping was applied to model the viscous damping (Chopra 2007). The transfer of the stiffness and resisting force of the rafter elements from the basic system to the global coordinate system was applied by corotational transformation. The uniaxial Material Steel 01 model was selected to predict the uniaxial steel material with kinematic hardening of 0.02. The fiber section was used to model the cross-sections of the frame by assigning defined geometry and material. This section provides the distributed plasticity capability for rafter and column elements. Nonlinear beam-column elements with distributed plasticity were used to model the rafters and columns. Shear deformations are also considered. In this study, overall buckling is considered using corotational transformation. To prevent local buckling, compact sections were used (see Table 1) in which the deterioration due to local buckling was negligible. Also, the ultimate strain of the steel in the critical fibers was controlled so that it did not exceed the ultimate limit.

To model the web-tapered members of the rafters and columns, prismatic microelements with variable depth were used, where six integration points were applied for each microelement. The depth difference between the two sections of adjacent microelements (Δh_0) was 0.02 m. Based on the defined Δh_0, the length and number of microelements (l_0 and n_0, respectively) for each member were determined. In the prismatic area of the rafters, the length of microelements equal to $2.5l_{0,r}$ was selected. The specifications of prismatic microelements are presented in Table 2. Also, dead loads on the rafters and columns as well as snow loads only on the rafters were applied concentratedly to each node according to the loading area. For a better understanding, a schematic view of the SGF model developed in OpenSees is shown in Figure 1(b). Figure 1(c) illustrates the deformations created in the SGF model under gravity loads. As shown in Figure 1(c), the SGF model developed in OpenSees, in addition to considering drifts of the member ends (Δ), the local deformation relative to the member chord between the end nodes (δ) is also incorporated, where the rafter has double curvature and the column has single curvature. After completing the nonlinear modeling process of SGFs developed in OpenSees, by performing eigenvalue analysis, the first-mode period of models A, B, C and D were obtained equal to 0.9, 1.53, 0.63 and 1.31 s, respectively. The mode shapes of the fundamental vibration modes of SGF model is shown in Figure 2. Validation of SGF model was presented by Malekizadeh et al. (2021b, 2022a).

Table 1. Section dimensions of the rafter and column members.

Model	Column web height at top (m)	Column web height at bottom (m)	Rafter web height at ridge (m)	Rafter web height at eave (m)	Web thickness (m)	Flange thickness (m)	Flange width (m)
A	0.8	0.3	0.4	0.8	0.008	0.010	0.18
B	1.0	0.3	0.5	1.0	0.010	0.012	0.24
C	1.5	0.3	1.0	1.5	0.014	0.018	0.34
D	1.5	0.3	1.0	1.5	0.014	0.020	0.40

Table 2. Specifications of prismatic microelements.

	Model A		Model B		Model C		Model D	
	Column	Rafter	Column	Rafter	Column	Rafter	Column	Rafter
Δh_0 (m)	0.02	0.02	0.02	0.02	0.02	0.02	0.02	0.02
l_0 (m)	0.24	0.10	0.34	0.08	0.10	0.24	0.20	0.24
n_0	2 × 25	2 × 53	2 × 35	2 × 66	2 × 60	2 × 66	2 × 60	2 × 66

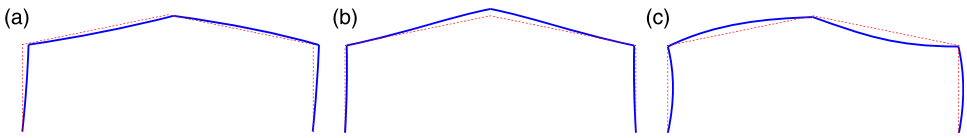

Figure 2. Fundamental vibration modes of SGF model (a) mode 1, (b) mode 2 and (c) mode 3.

Selection of ground motion sequences

According to Shome and Cornell (1999), the use of 10 to 20 ground motions often leads to acceptable accuracy in damage estimation. Silwal and Ozbulut (2018) and Bao et al. (2019) used 10 real seismic sequences to investigate the effects of aftershocks on the fragility of structures. In this regard, the present study selected a set of 10 real ground motion sequences from the PEER-NGA database (2006) for nonlinear dynamic analyses. Each seismic sequence consists of a mainshock and one corresponding aftershock selected from the same station. Since these seismic sequences occur naturally, aftershocks have inherent characteristics affected by the mainshocks. It should be noted that the current study identifies the initial seismic event as the mainshock and subsequent event as the aftershock. A mainshock is generally considered to be the earthquake with the highest magnitude or intensity, while aftershocks are earthquakes that occur after the mainshock. The magnitudes of mainshock and aftershock events were considered to be greater than 5.5 and 5.0, respectively. The ground motion sequences used in this study were selected with tectonic characteristics of Class D soil because the SGF models were located on Class D soil. The characteristics of the selected ground motion sequences are presented in Table 3. In particular, magnitude (M), source-to-site distance (R), shear wave velocity at top 30 m (V_{S30}), peak ground acceleration (PGA), arias intensity (AI) and duration for each seismic event are provided in the table.

Figure 3 demonstrates the 5% damped spectral response acceleration of the individual ground motions, which were generated by Seismosignal software. The acceleration time history for the seismic sequence of S1 is also shown in Figure 4. As can be seen, a time interval of 40 s was considered by adding zero acceleration values between the mainshock and aftershock ground motions to ensure stabilized response under the free vibration of the structures before the occurrence of aftershock. besides, a time interval of 40 s with zero acceleration values was added at the end of the aftershock ground motions to allow the structure to damp the earthquake energy and vibration after the occurrence of the second event. Since a finite number of seismic sequences are used in the analyses, efficiency and sufficiency are the main features of an optimal IM, which are discussed next.

Mainshock IDA analysis

Overview

In the IDA analysis, the structural model is subjected to a set of ground motions that are scaled from a very low level with incremental steps through nonlinear response history analyses until a high level where the collapse of the structure occurs (Vamvatsikos and Cornell 2002). Before performing the nonlinear time history analysis at each step of the IDA analysis, static analysis is conducted under gravity loads. Due to the specific geometrical properties of SGFs, gravity loads produce an initial horizontal drift in the shoulder. Hence, SFG models in the initial state experience a static drift due to gravity loads. After incorporating the ground motion, the absolute maximum drift for SFGs includes initial static drift due to gravity loads plus maximum dynamic drift due to ground motion. Since in SGFs both column and rafter drifts can be selected as a criterion, but here because seismic sequences are applied to the frames in a horizontal direction, only drift in the column is considered as a criterion.

IDA curves

In order to determine the collapse capacity and identify the damage states for the aftershock IDA analysis, an IDA analysis is first performed using the only mainshock ground motions. To perform the mainshock IDA analysis on SGFs, the first step is to select the appropriate IM and damage measure (DM). Herein, in IDA analysis on SGFs, the 5% damped first-mode spectral acceleration ($Sa(T_1,5\%)$) and the transient absolute maximum drift angle ($\Theta_{T-a,max}$) are used as IM and DM, respectively. According to FEMA 356 (2000), the collapse limit state associated with $\Theta_{T-a,max}$ is considered to be 5% in the mainshock IDA analysis. The IDA curves of SGFs subjected to mainshock only are shown in Figure 5, where $\Theta_{T-a,max}$ appears in the IDA curves as an absolute value. Also, the mainshock damage states are selected to be 0.7% (DS0), 2.5% (DS1) and 3.75% (DS2). It should be noted that 0.7% and 2.5% $\Theta_{T-a,max}$ are correspond to immediate occupancy and life safety limit states in FEMA 356 (2000), where 3.75% $\Theta_{T-a,max}$ is related to the average limit states of collapse prevention and life safety. By comparing the 50% mainshock IDA curves shown in Figure 5, it is evident that models A and C (short-period SGFs) have a higher collapse

Table 3. Characteristics of selected ground motion sequences.

No.	Event name	Station	Sequence	Time	M	R (km)	V_{S30} (m/s^2)	PGA (g)	AI (m/sec)	Duration (sec)
S1	USA: Hollister	Hollister city Hall	Main	1961-04-09	5.60	18.08	198.77	0.070	0.100	87.560
			After	1961-04-09	5.50			0.115	0.199	40.465
S2	USA: Coalinga	Pleasant Valley P.P. - yard	Main	1983-05-02	6.36	8.41	257.38	0.602	4.127	58.140
			After	1983-07-22	5.77			0.575	0.799	21.720
S3	USA: Northridge	LA - Century city CC North	Main	1994-01-17	6.69	23.41	277.98	0.256	1.178	39.940
			After	1994-01-17	6.05			0.111	0.067	19.940
S4	USA: Mammoth Lakes	Mammoth Lakes H. S.	Main	1980-05-25	6.06	4.67	346.82	0.243	0.798	29.980
			After	1980-05-25	5.69			0.442	1.265	29.980
S5	Italy: Irpinia	Bovino	Main	1980-11-23	6.90	46.25	356.39	0.046	0.041	38.457
			After	1980-11-23	6.20			0.033	0.015	23.890
S6	Taiwan: Chi-Chi	HWA034	Main	1999-09-20	7.62	44.32	379.18	0.137	0.434	89.985
			After	1999-09-25	6.30			0.059	0.056	77.980
S7	China: Northwest China	Jiashi	Main	1997-04-11	6.10	17.73	240.09	0.273	0.770	59.940
			After	1997-04-15	5.80			0.239	0.382	59.940
S8	Nicaragua: Managua	ESSO	Main	1972-12-23	6.24	4.06	288.77	0.330	2.009	45.675
			After	1972-12-23	5.20			0.221	0.350	47.875
S9	Italy: Friuli	Codroipo	Main	1976-05-06	6.50	33.40	249.28	0.091	0.131	39.955
			After	1976-09-15	5.91			0.019	0.013	33.550
S10	USA: Whittier Narrows	LA - Obregon Park	Main	1987-10-01	5.99	15.18	349.43	0.428	1.049	39.975
			After	1987-10-04	5.27			0.344	0.439	21.980

capacity than models B and D (long-period SGFs), which similar observations were reported by Malekizadeh et al. (2021b, 2022a, 2022b). The results of the mainshock IDA analysis are used to determine the required scale factors associated with the mainshock damage states during the aftershock IDA analysis, which are discussed next.

Testing the efficiency-sufficiency of IM

To test the efficiency of IM, one-parameter log-log linear regression of DM on IM is used, as defined in equation (1):

$$\boldsymbol{ln(DM) = ln(a) + b.ln(IM) + \varepsilon} \tag{1}$$

where a and b are the regression coefficients and ε is the regression residual. Therefore, the median DM given IM (DM_{mdn}) can be calculated as follows:

$$\boldsymbol{ln(DM_{mdn}) = ln(a) + b.ln(IM)} \tag{2}$$

Effectiveness of a demand model is determined by its ability to evaluate equation (2) in a closed form. In order to accomplish this task, it is assumed that the DMs follow log-normal distributions. The dispersion (σ), accounting for the uncertainty in the relation that is contingent upon the IM, is estimated using equation (3):

$$\boldsymbol{\sigma = \sqrt{\frac{\sum_{i=1}^{n}[(ln(DM) - ln(DM_{mdn})]^2}{n-2}}} \tag{3}$$

where n is the number of simulations.

The ability of an IM to anticipate the structural response with low dispersion is called efficiency. The efficiency of IM in DM prediction can be evaluated via the conditional standard deviation of DM, σ. Use of an efficient IM reduces σ and, consequently, increases the reliability of the seismic performance assessments of the structures. In other words, the IM that can predict the structural response with low dispersion can be regarded as an efficient IM. Figure 6 shows the PSDMs for the studied SGFs. Each figure depicts the corresponding linear regression equation and σ value. As shown in this figure, in all models, the use of $Sa(T_1,5\%)$ leads to low dispersion and high efficiency. These observations support the results of Malekizadeh et al. (2021b).

In addition to the fact that an optimal IM should be sufficient, it is necessary to check the sufficiency of the considered IM. The sufficiency of an IM for predicting the structural response implies that the distribution of the structural response obtained based on the IM is independent of ground motion characteristics, such as magnitude (M) and source-to-site distance (R). Since a finite number

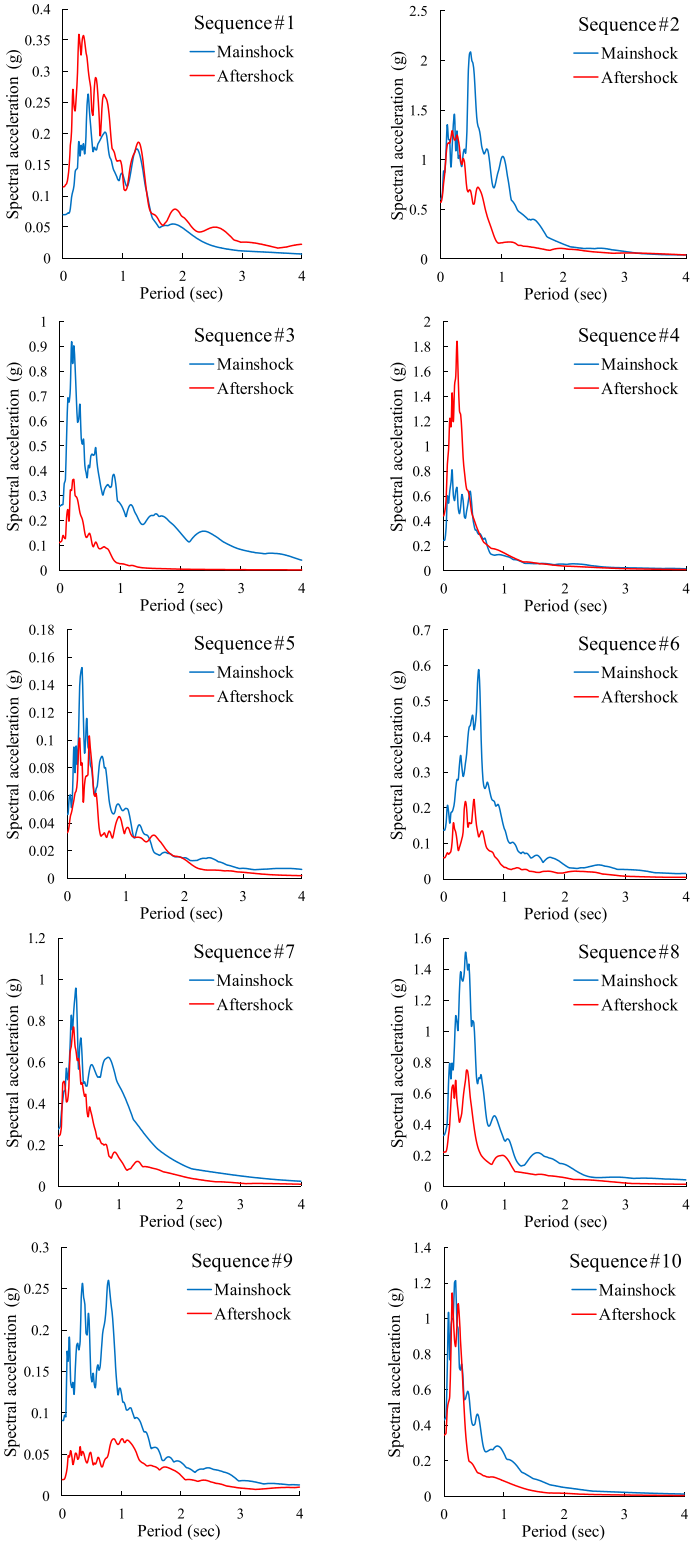

Figure 3. The 5% damped spectral response acceleration of selected ground motion sequences.

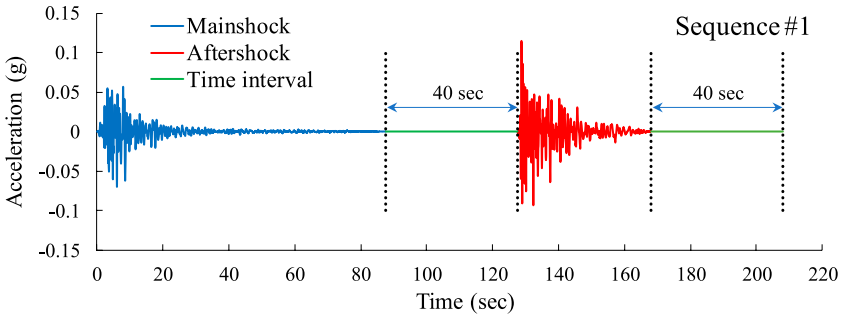

Figure 4. Acceleration time history for seismic sequence of S1.

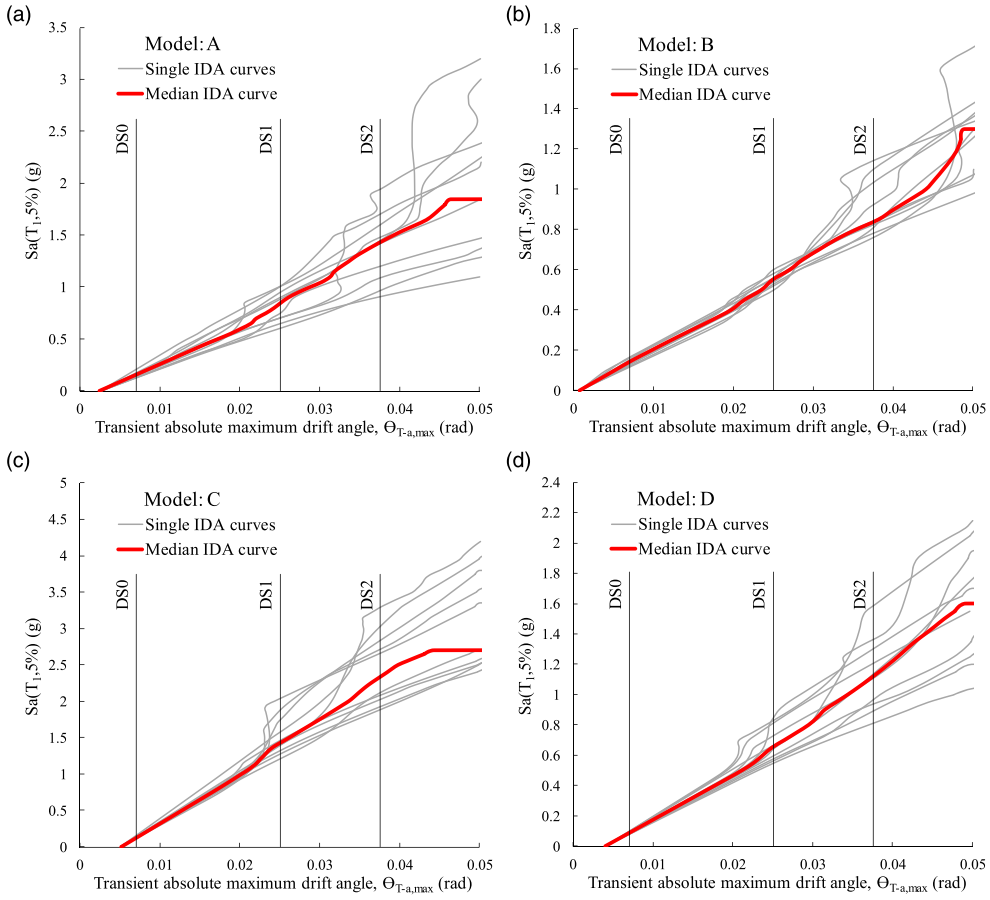

Figure 5. Mainshock IDA curves for (a) model A, (b) model B, (c) model C and (d) model D.

of analyses are used in order to obtain the distribution of the structural response, sufficiency is one of the main features of an optimal IM. In fact, if the obtained distribution is dependent on M and R values of the used ground motion records and their distribution in the structural response analyses is not the same as that of the ground motions that will occur at the site in the future, it can be concluded that the distribution will be biased (Bradley et al., 2010; Yakhchalian et al., 2015). Using a sufficient IM can decouple the seismic hazard analysis from structural response analysis.

In order to investigate the sufficiency of IM with respect to M and R for predicting DM, linear regression can be used between the regression residuals obtained from equation (1) and these ground motion characteristics as:

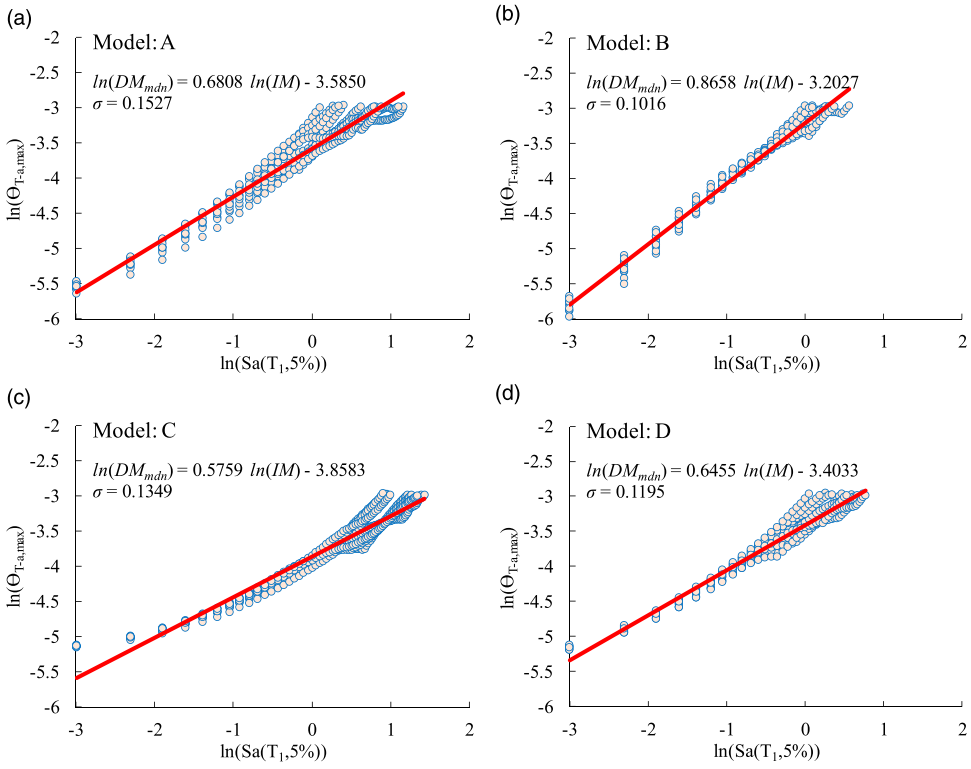

Figure 6. Testing the efficiency of IM for (a) model A, (b) model B, (c) model C and (d) model D.

$$ln(\varepsilon_{mdn}) = ln(a) + b.x \tag{4}$$

where ε_{mdn} is the median value of ε; a and b are the estimated coefficients of the linear regression, and x is M or the natural logarithm of R. Because the linear regression is based on a finite number of observations, testing the statistical significance of b is essential. The F-test can be applied to test the statistical significance of b. Generally, a *p-value* less than 0.05 obtained from the F-test proves that b is statistically significant, implying the insufficiency of the IM, which was already applied in order to obtain the structural response distribution, with respect to x (Bradley et al., 2010; Yakhchalian et al., 2015). Figures 7 and 8 display the results of testing the sufficiency of IM with respect to M_{MS} and R, respectively, for predicting DM on the studied SGFs. Each figure depicts the corresponding linear regression equation and *p-value* value. As demonstrated in this figure, IM can predict DM in the case of all models independent of M_{MS} and R, because the obtained *p-value* is greater than 0.05. In other words, IM is sufficient with respect to M_{MS} and R for predicting DM on all models.

Aftershock IDA analysis

Overview

The damages due to the mainshock can significantly affect the seismic performance of the structure at subsequent excitations (Bojórquez and Ruiz-García 2013; Uma et al., 2010). In this regard, in the present study, three mainshock damage states based on $\Theta_{T-a,\,max}$ is considered for the aftershock fragility assessment of SGFs. These damage states are representing minor, moderate and severe damage of frames under mainshock ground motions. In other words, three scenarios for the mainshock are considered in the aftershock IDA analysis. Also, the post-mainshock damage state was considered to be 5% (i.e., collapse limit state) in the aftershock IDA analysis. Malekizadeh et al. (2021b) showed that the initial drift angle created due to gravity loads causes SGFs to experience the immediate occupancy limit state under very low earthquake intensity and this limit state can be ignored in evaluating the seismic behavior of such structures. Hence, here DS0 is expected to have a negligible level of mainshock damage, so that the structure remains intact. In the next section, this case will be examined in detail.

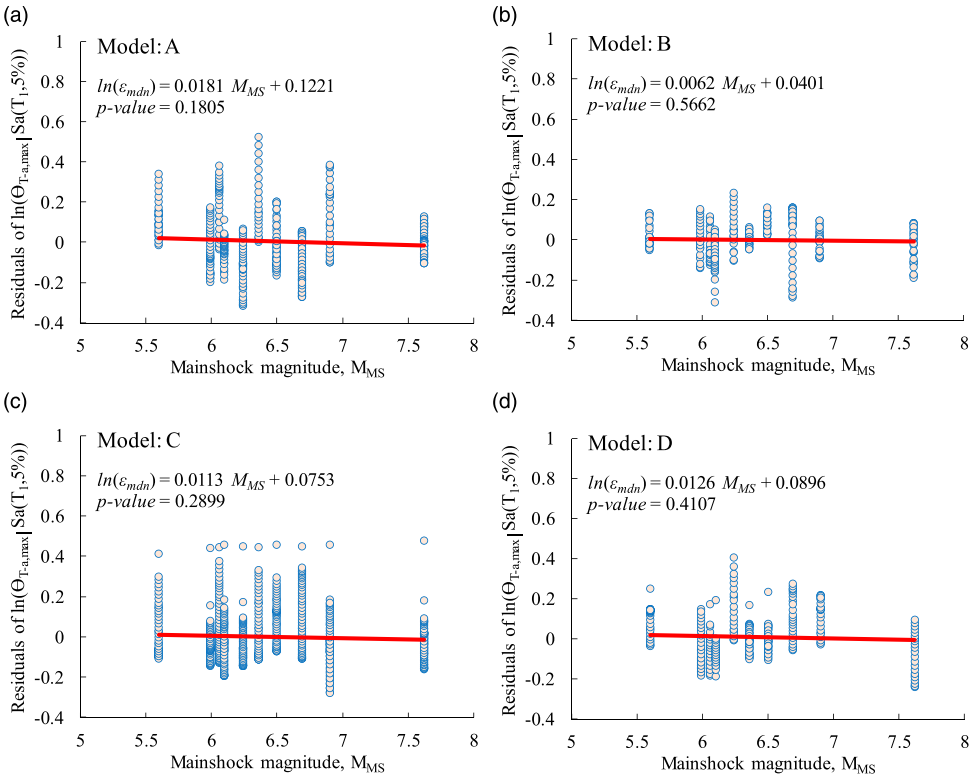

Figure 7. Testing the sufficiency of IM with respect to mainshock magnitude (M_{MS}) for (a) model A, (b) model B, (c) model C and (d) model D.

IDA curves

To develop the aftershock IDA curves, the nonlinear response history analyses of SGFs are performed first under mainshock ground motions scaled to damage states corresponding to 0.7%, 2.5%, or 3.75% $\Theta_{T-a,max}$. Then with the elapsed time of 40 s at the end of mainshock, to ensure the rest of the frame between the mainshock and aftershock, aftershock ground motions are scaled from a very low level with incremental steps through nonlinear response history analyses until the collapse of the structure occurs during the aftershock (i.e., $\Theta_{T-a,max}$ = 5%), while at each step of the analysis, the mainshock scale factor is kept constant. It should be noted that to achieve maximum damage of SGFs at each step of the aftershock IDA analysis, aftershock ground motions were applied once in the positive direction and again in the negative direction, while the direction of the mainshock was assumed to be constant. Consequently, the maximum response of the structure in the two mentioned cases was considered as the final response of the structure at each step of the aftershock IDA analysis. Figure 9 shows the time history of the column drift angle for model D subjected to the seismic sequence of S4. Here, the mainshock ground motion is scaled such that the model D reaches DS1, and then the aftershock ground motion is applied to the model D frame with scale factors of 1.0 g and −1.0 g.

The aftershock IDA curves for SGFs subjected to three different mainshock damage states during mainshock are illustrated in Figure 10. It is observed that the aftershock IDA curves for SGFs have a vertical line at low intensity levels of aftershock ground motions, indicating the $\Theta_{T-a,max}$ of the frames is controlled by the mainshock for low intensity aftershocks.

Figure 11 shows the aftershock IDA curve #1 for the intact and pre-damaged model D. As can be seen in this figure, DS0 has a negligible level of mainshock damage, such that it follows a completely similar behavior compared to the aftershock IDA curve related to intact state (i.e., mainshock = 0), while DS1 and DS2 visibly reduce the capacity of the structure. Therefore, DS0 is considered an intact state of the structure.

Testing the efficiency-sufficiency of IM

To examine the impact of aftershocks on structural response, four SGFs were subjected to seismic sequences. As mentioned in Section 5.2, aftershocks applied in the positive and negative directions were employed, and the

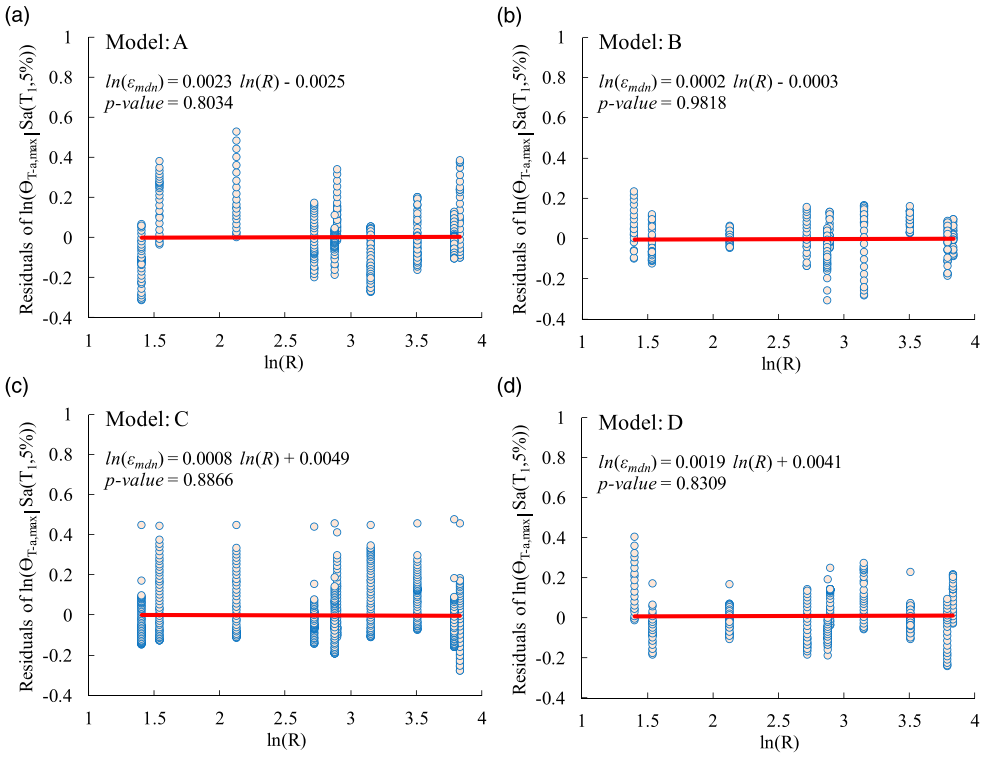

Figure 8. Testing the sufficiency of IM with respect to source-to-site distance (R) for (a) model A, (b) model B, (c) model C and (d) model D.

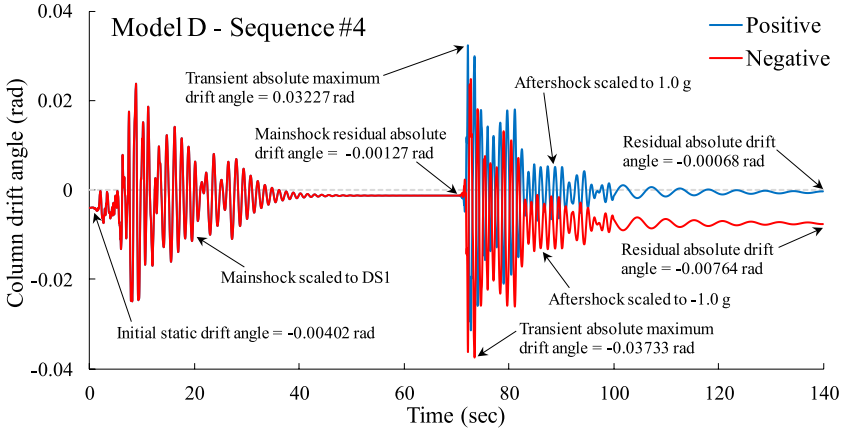

Figure 9. The effect of aftershock direction on the response of model D subjected to seismic sequence of S4.

mainshock motion was scaled to achieve three different damage states: intact (DS0) and damaged (DS1 and DS2). Then, aftershock IDA analyses on pre-damaged structures were performed. Analysis data were used to develop the aftershock PSDMs. Figure 12(a) depicts a linear aftershock PSDM fit to the DS1 data set. These data show that for the damaged frame DS1, a linear model does not provide a good fit to the entire data set in a log-transformed space. If a linear model is used, aftershock demand and damage states are underestimated for higher and lower $Sa(T_1,5\%)$ values. In particular, for DS1, $\ln(\Theta_{T-a,\max})$ is constant for small $Sa(T_1,5\%)$ (i.e., small magnitude) aftershocks because the final damage state of the structure is determined by the larger intensity mainshock. If the linear regression model is

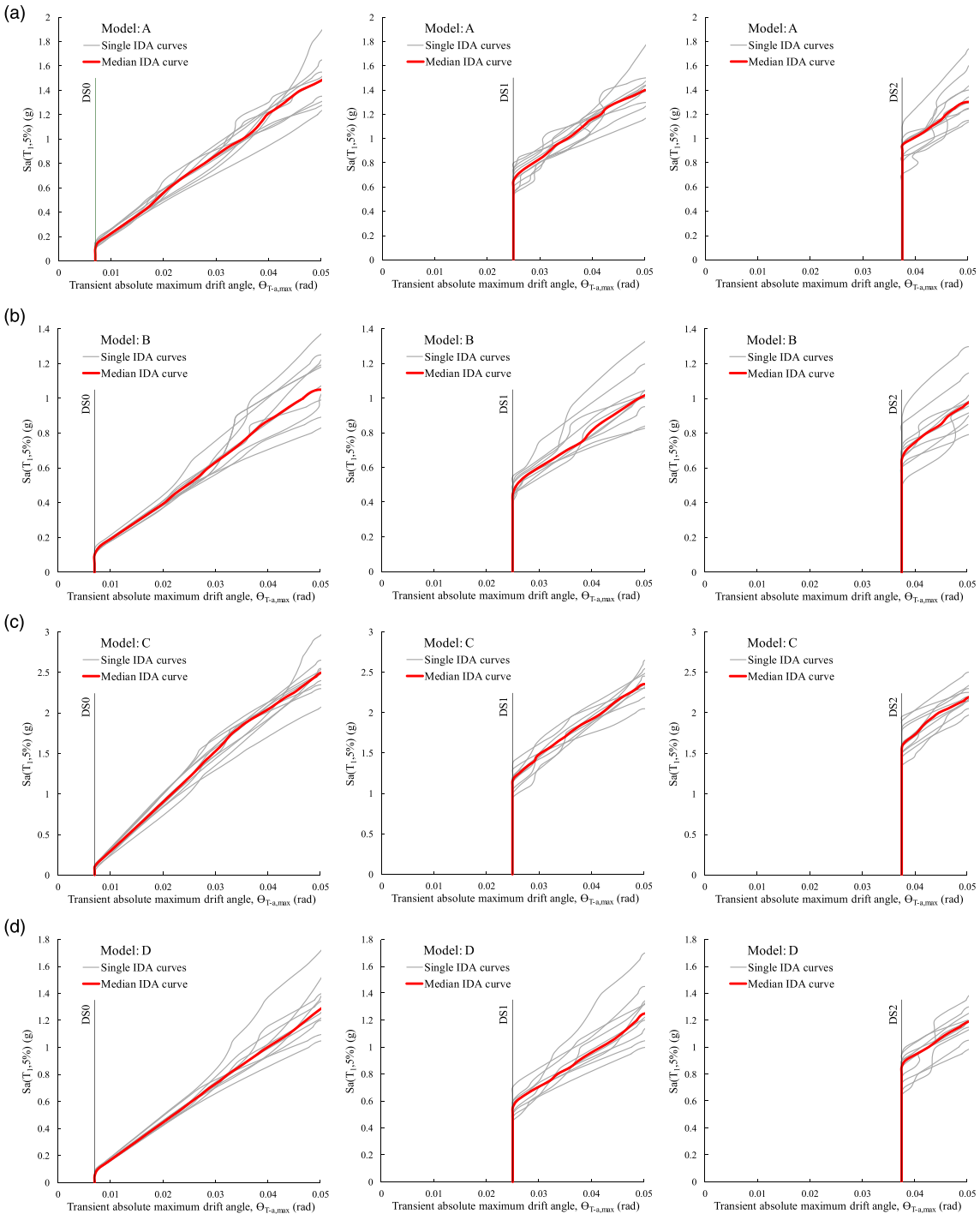

Figure 10. Aftershock IDA curves at three different mainshock damage states for (a) model A, (b) model B, (c) model C and (d) model D.

used to define the aftershock PSDM for DS1, crossover fragility curves are achieved. These crossover fragilities indicate that for aftershocks with higher Sa(T_1,5%), structures that are lightly to moderately damaged during the mainshock have a higher probability of reaching a given damage state than structures that are severely damaged during the mainshock. To better represent the aftershock DM-IM data and prevent crossover fragility curves, a bilinear aftershock PSDM was adopted. The breaking point of this model was determined by minimizing the sum of the square of residuals between actual and fitted values (Jeon et al., 2015a; Jeon, 2013). Figure 12(b) shows a bilinear aftershock PSDM fit to the DS1 data set. This bilinear model comprises a first branch with a zero slope and a second branch with a much steep slope; thus, the model indicates that aftershock intensity has no impact on demand or damage for small-intensity aftershocks, but significant impact for large-intensity aftershocks. Given this and the observation discussed earlier that a linear model, fit to data above the break point, provides adequate characterization of risk for the range of interest, the bilinear model was replaced by a linear model fit to the data above the break point in the bilinear model. The unknown parameters (a, b, and σ) of the aftershock PSDMs for each mainshock damage state resulting from the second branch of the bilinear model are presented in Table 4. As demonstrated in this table, in all models, the use of Sa(T_1,5%) leads to low dispersion and, thus, high efficiency; therefore, σ in models A and C is higher than that in models B and D. Also, the results of testing the sufficiency of IM with respect to M_{AS} and R, respectively, for predicting DM on the studied SGFs for each mainshock damage state resulting from the second branch of the bilinear model are presented in Table 5. As shown in this table, IM can predict DM on all models independent of M_{AS} and R, because the obtained *p-value* is greater than 0.05. In other words, IM is sufficient with respect to M_{AS} and R for predicting DM on all models.

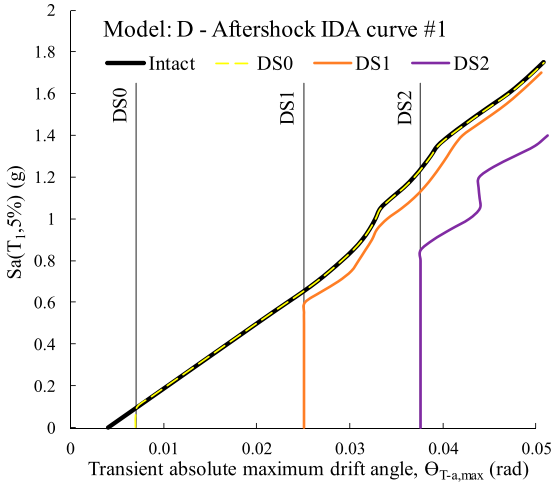

Figure 11. Aftershock IDA curve #1 for intact and pre-damaged model D.

Results and discussion

Transient absolute maximum drift angle

Currently, fragility functions used in performance-based earthquake engineering are defined by a single cumulative probability function. Accounting for the initial damage state of a structure after a mainshock (DS_{MS}), aftershock fragility function defines the probability that a damaged structure will exceed a particular damage state when subjected to an aftershock of intensity, as defined in equation (5):

$$P[DM_{AS} > C | IM_{AS}, DS_{MS}] = \Phi\left[\frac{DM_{mdn,AS}/DM_{mdn,C}}{\sqrt{\sigma_{AS}^2 + \sigma_C^2 + \sigma_M^2}}\right] \quad (5)$$

where DM_{AS} is the aftershock demand for an ID_{MS}; $DM_{mdn,AS}$ and σ_{AS} are the median value and dispersion of the aftershock demand as a function of IM_{AS} for a DS_{MS}; $DM_{mdn,C}$ and σ_C are the median value and dispersion of the structural capacity associated with the aftershock state; the

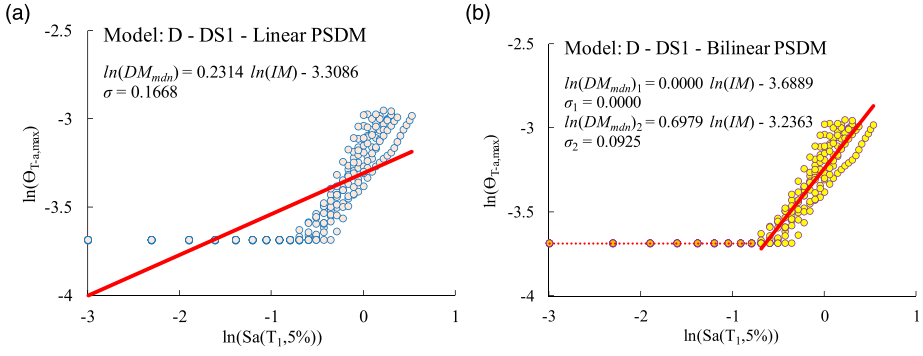

Figure 12. Aftershock PSDM fit to the DS1 (a) linear and (b) bilinear.

Table 4. Testing the efficiency of IM for each mainshock damage state resulting from the second branch of the bilinear model.

Model	Mainshock damage state	*a*	*b*	σ
A	DS0	0.0342	0.8345	0.0955
	DS1	0.0358	0.7552	0.0935
	DS2	0.0412	0.4015	0.0804
B	DS0	0.0442	0.8766	0.0903
	DS1	0.0448	0.7489	0.0919
	DS2	0.0461	0.3700	0.0739
C	DS0	0.0230	0.7123	0.0978
	DS1	0.0226	0.8575	0.0946
	DS2	0.0300	0.5575	0.0819
D	DS0	0.0380	0.7481	0.0916
	DS1	0.0393	0.6979	0.0925
	DS2	0.0433	0.4344	0.0760

Table 5. Testing the sufficiency of IM with respect to M_{AS} and R for each mainshock damage state resulting from the second branch of the bilinear model.

		p-value	
Model	Mainshock damage state	M_{AS}	R
A	DS0	0.5358	0.2111
	DS1	0.6817	0.0892
	DS2	0.1137	0.0611
B	DS0	0.4437	0.2790
	DS1	0.7449	0.0573
	DS2	0.3014	0.0756
C	DS0	0.1148	0.2489
	DS1	0.0704	0.4097
	DS2	0.0692	0.1935
D	DS0	0.2484	0.0782
	DS1	0.3470	0.6945
	DS2	0.5115	0.1191

modeling uncertainty, σ_M. Ellingwood et al. (2007) recommended $\sigma_M = 0.2$ on the basis of the assumption that the frame model predicts the actual response of frames with ±30% error at a confidence level of 90%. Two assumptions are made for deriving the aftershock fragility function of equation (5): (1) the aftershock intensity is independent of the mainshock intensity and (2) the correlation between aftershock and mainshock intensities is not incorporated in the framework.

Figure 13 shows the aftershock fragility curves for each mainshock damage state resulting from the second branch of the bilinear model, where the post-mainshock damage state was considered to be 5% (i.e., collapse limit state). This figure illustrates the relative vulnerability of SGFs at different mainshock damage states over a range of aftershock intensities. Jeon et al. (2015b) showed that in the aftershock fragilities for higher post-mainshock damage states, the curves determined using the bilinear model are the same as those obtained from a linear model fit to the DM-IM data above the break point. SGFs subjected to different mainshock damage states are compared in terms of the relative change in the aftershock collapse capacity which indicates the $Sa(T_1,5\%)$ associated with a 50% probability of reaching the collapse limit state in aftershock fragility curves. Table 6 provides the aftershock collapse capacity of SGFs at each mainshock damage state. The value of aftershock collapse capacity reduction for intact SGFs compared to damaged ones is also presented in Table 6.

According to Figure 13 and Table 6, it is evident that all SGFs with low damages from the mainshock experience somewhat small reductions in their aftershock collapse capacity, while the effect of aftershocks becomes more pronounced when the structural damage during the mainshock increases. For example, the aftershock collapse capacity of the model D for intact state compared to DS1 and DS2 (damaged) decreased 3.9% and 9.3%, respectively. Similar observations for the conventional steel frames were reported in previous studies (Li et al., 2014; Ribeiro et al., 2014). Besides, an interesting behavior is observed at all mainshock damage states, where models A and C (short-period SGFs) have a higher aftershock collapse capacity than models B and D (long-period SGFs). For example, model C, which has the shortest period among other models, has 40%, 56% and 46% more aftershock collapse capacity in DS2 compared to models A, B and D, respectively. Also, the median collapse capacity of models A and C (short-period SGFs) on average in all mainshock damage states are 1.39 g and 2.34 g, respectively, while the corresponding capacities for models B and D (long-period SGFs) are 1.01 g and 1.23 g, respectively.

Residual absolute drift angle

Control of the residual drift angles at the end of seismic sequences is essential not only for the seismic performance assessment of pre-damaged structures but also for the decision on whether to retrofit or repair them. To plot median IDA curves, residual absolute drift angle (Θ_{R-a}) is used here as DM, where absolute means that there is an initial gravity drift in the SGF models that are considered in the analyses. As explained in Section 3, the two-time intervals were considered at each seismic sequence: the first between the mainshock and aftershock, and the second at the end of aftershock ground motion to ensure the residual response stabilized under the free vibration of the structures. Θ_{R-a} in the aftershock IDA curves at the end of the second time interval is recorded at each step of the analysis. According to FEMA P-58 (2000), structures that experience residual drift angles over 1% require major realignment and those with residual drift angles greater than 2% cannot be repaired. SGFs that

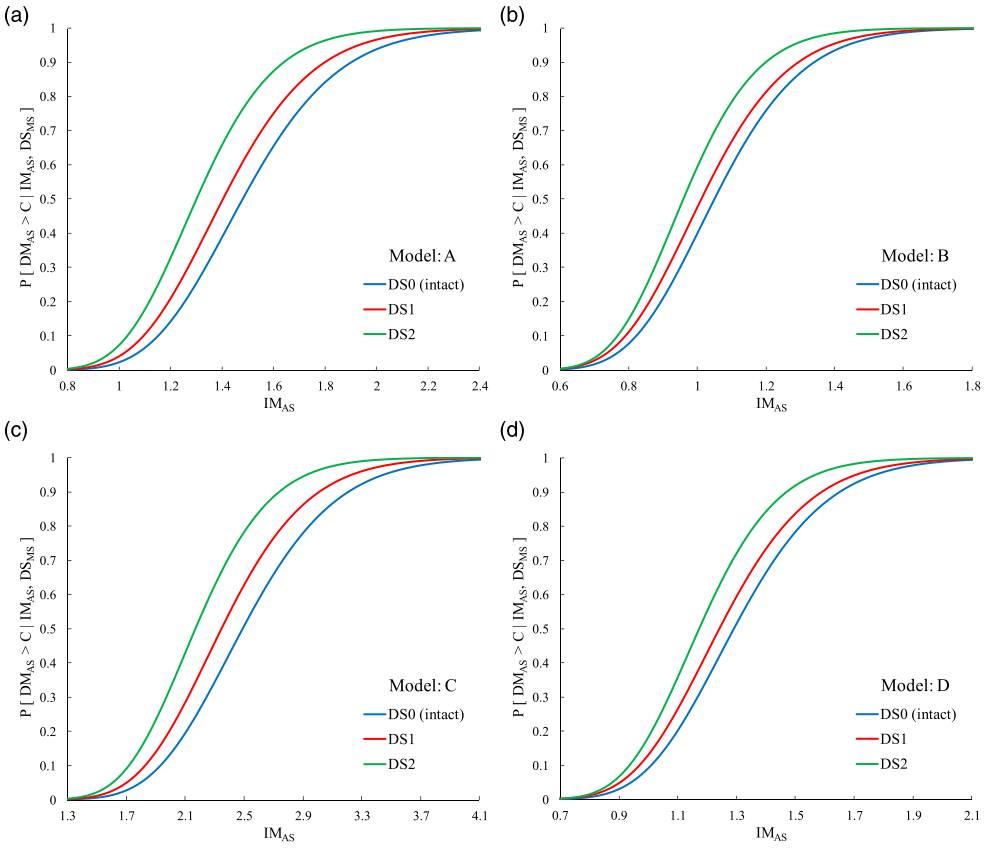

Figure 13. Aftershock fragility curves for each mainshock damage state resulting from the second branch of the bilinear model for (a) model A, (b) model B, (c) model C and (d) model D.

Table 6. Aftershock collapse capacity of SGFs at each mainshock damage state.

	Aftershock collapse capacity (g)			Decrease in aftershock collapse capacity	
Model	DS0 (intact)	DS1	DS2	DS1	DS2
A	1.48	1.40	1.30	5.4%	12.2%
B	1.05	1.01	0.96	3.8%	8.6%
C	2.49	2.35	2.17	5.6%	12.9%
D	1.29	1.24	1.17	3.9%	9.3%

were subjected to the seismic sequence, are compared here in terms of the relative change of the aftershock collapse capacity associated with the major realignment and demolition in the median IDA curves for Θ_{R-a}. Note that the aftershock collapse capacity associated with the major realignment and demolition indicates the Sa(T_1,5%) related to 1% and 2% Θ_{R-a}, respectively. Figure 14 shows the median IDA curves of SGFs at different mainshock damage states for Θ_{R-a}. It is obvious that Θ_{R-a} in median IDA curves is an absolute value and always appears positive.

It is clear from Figure 14 that at the same intensity levels, all SGFs experience a higher Θ_{R-a} in DS1 and DS2 (damaged) compared to intact state. The aftershock collapse capacity associated with the demolition for model A is 1.40 g, 1.35 g and 1.25 g for DS0 (intact), DS1 and DS2 damage states, respectively. The aftershock collapse capacity associated with the demolition for model C is 2.30 g, 2.15 g and 2.10 g for DS0 (intact), DS1 and DS2 damage states, respectively. It should be noted that these values are lower than the aftershock collapse capacity of models A and C at each of these damage states. However, for models B and D, Θ_{R-a} does not exceed 2% at the aftershock collapse capacity of the structure. In the aftershock collapse capacity of the structure, model C experiences the most Θ_{R-a} among other models, while Model B barely exceeds 1% Θ_{R-a}.

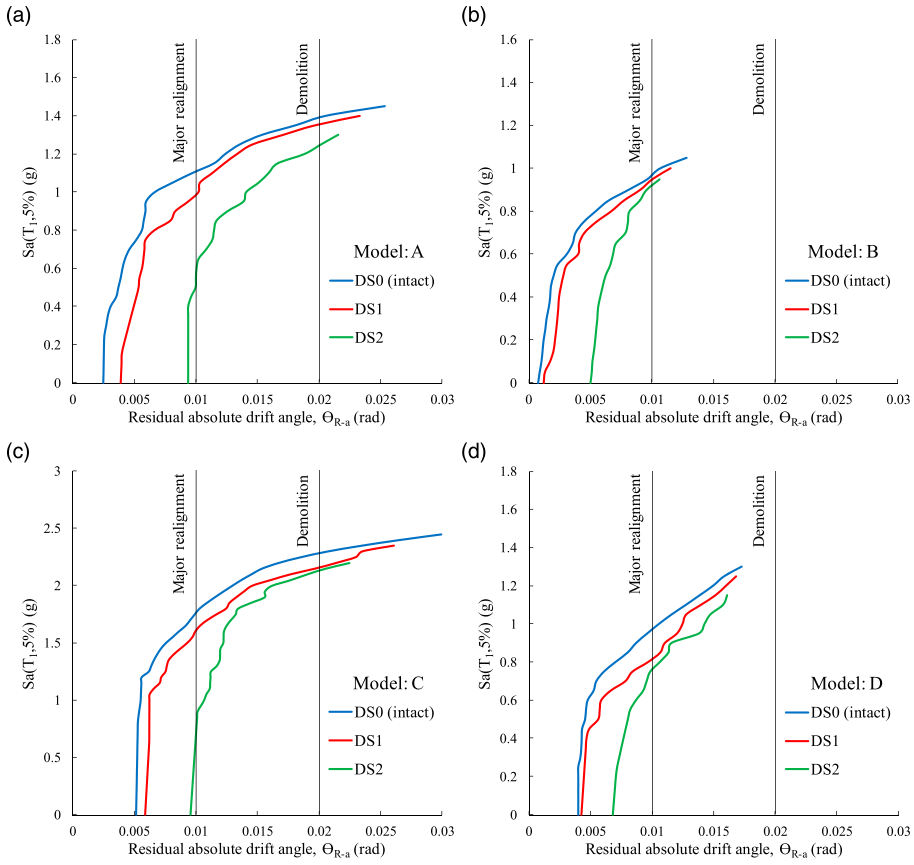

Figure 14. Median IDA curves for the residual absolute drift angle at different mainshock damage states for (a) model A, (b) model B, (c) model C and (d) model D.

Conclusion

In the present study, mainshock IDA analysis was first conducted on four SGFs. Then mainshock damage states based on the transient absolute maximum drift angle were considered, and aftershock IDA analysis was performed on the mainshock-damaged structures. Aftershock fragility curves using PSDMs for transient absolute maximum drift angle and median IDA curves for residual absolute maximum drift angle were developed to compare intact and pre-damaged SGFs.

The outputs prove that $Sa(T_1,5\%)$ as a prevalent IM can efficiently and sufficiently predict $\Theta_{T-a,max}$ on SGFs under seismic sequences. Besides, an interesting behavior was observed at all mainshock damage states, where the demand sensitivity in models A and C (short-period SGFs) was higher than models B and D (long-period SGFs). Also, the results showed that aftershocks significantly increase the vulnerability of SGFs, especially when they had short periods, where for the largest mainshock damage state (i.e., DS2) compared to the intact state, the aftershock collapse capacity of models A and C (short-period SGFs) were decreased by 12.2% and 12.9%, respectively. However, the corresponding capacities for models B and D (long-period SGFs) were reduced by 8.6% and 9.3%, respectively. Despite the greater reduction in the aftershock collapse capacity of short-period SGFs, they were more vulnerable than long-period SGFs under seismic sequences. Moreover, in all SGFs that had low damage from the mainshock, they experienced somewhat small reductions in their aftershock collapse capacity, while the effect of aftershocks became more apparent with increasing structural damage during the mainshock. On the other hand, it was found that residual drift angle control is very important for short-period SGFs under seismic sequences, because before the collapse of the structure with the transient drift angle, models A and C with the residual drift angle had led to demolition. Long-period SGFs have the potential to lower the post-earthquake losses by minimizing the residual drift angles and thereby satisfying a reparability state, where models B and D successfully control the residual drift angles and limit the residual drift

angles below 2%. By reducing residual drift angles, the post-earthquake of the structure performance will increase and the cost of repair will decrease. Therefore, it is recommended that seismic design codes in dealing with short-period SGFs pay more attention to the effects of seismic sequences. Also, in the aftershock fragility assessment of short-period SGFs, control of residual drift angles should be considered seriously.

Declaration of conflicting interests

The author(s) declared no potential conflicts of interest with respect to the research, authorship, and/or publication of this article.

Funding

The author(s) received no financial support for the research, authorship, and/or publication of this article.

Orcid iDs

Mohammad Malekizadeh https://orcid.org/0000-0002-2200-143X
Nader Fanaie https://orcid.org/0000-0002-6789-8930

References

Alliard PM and Léger P (2008) Earthquake safety evaluation of gravity dams considering aftershocks and reduced drainage efficiency. *Journal of Engineering Mechanics* 134: 12–22. DOI: 10.1061/(ASCE)0733-9399(2008)134:1(12)

Amiri S and Bojórquez E (2019) Residual displacement ratios of structures under mainshock-aftershock sequences. *Soil Dynamics and Earthquake Engineering* 121: 179–193. DOI: 10.1016/j.soildyn.2019.03.021

Bao X, Zhang MH and Zhai CH (2019) Fragility analysis of a containment structure under far-fault and near-fault seismic sequences considering post-mainshock damage states. *Engineering Structures* 198: 109511. DOI: 10.1016/j.engstruct.2019.109511

Bojórquez E and Ruiz-García J (2013) Residual drift demands in moment-resisting steel frames subjected to narrow-band earthquake ground motions. *Earthquake Engineering & Structural Dynamics* 42(11): 1583–1598. DOI: 10.1002/eqe.2288

Bradley BA, Dhakal RP, MacRae GA, et al. (2010) Prediction of Spatially distributed seismic demands in specific structures: ground motion and structural response. *Earthquake Engineering and Structural Dynamics* 39(5): 501–520. DOI: 10.1002/eqe.954

Chen X, Xiang N, Guan Z, et al. (2022) Seismic vulnerability assessment of tall pier bridges under mainshock-aftershock-like earthquake sequences using vector-valued intensity measure. *Engineering Structures* 253: 113732. DOI: 10.1016/j.engstruct.2021.113732

Chopra AK (2007) Dynamics of Structures: Theory and Applications to Earthquake Engineering. Englewood Cliffs, NJ, USA: Prentice-Hall.

Ellingwood BR, Celik OC and Kinali K (2007) Fragility assessment of building structural systems in Mid-America. *Earthquake Engineering and Structural Dynamics* 36(13): 1935–1952. DOI: 10.1002/eqe.693

FEMA 356 (2000) *Prestandard and Commentary for the Seismic Rehabilitation of Buildings*. Washington DC, USA: Federal Emergency Management Agency.

FEMA P-58 (2000) Seismic Performance Assessment of Buildings. Washington DC, USA: Federal Emergency Management Agency.

Feng W, Lindsey E, Barbot S, et al. (2017) Source characteristics of the 2015 M-w 7.8 Gorkha (Nepal) earthquake and its M-w 7.2 aftershock from space geodesy. *Tectonophysics* 712: 747–758.

Ge H, Chen X and Kang L (2012) Demand on stiffened steel shear panel dampers in a rigid-framed bridge pier under repeated seismic ground motions. *Advances in Structural Engineering* 15(3): 525–546. DOI: 10.1260/1369-4332.15.3.525

Ghasemi M, Khorshidi H and Fanaie N (2021) Performance evaluation of RC-MRFs with UHPSFRC and SMA rebars subjected to mainshock-aftershock sequences. *Structures* 32: 1871–1887. DOI: 10.1016/j.istruc.2021.02.058

Han R, Li Y and van de Lindt J (2014) Seismic risk of base isolated non-ductile reinforced concrete buildings considering uncertainties and mainshock–aftershock sequences. *Structural Safety* 50: 39–56. DOI: 10.1016/j.strusafe.2014.03.010

Han R, Li Y and Lindt JW (2015) Assessment of seismic performance of buildings with incorporation of aftershocks. *Journal of Performance of Constructed Facilities* 29(3): 04014088. DOI: 10.1061/(ASCE)CF.1943-5509.0000596

Hirose F, Miyaoka K, Hayashimoto N, et al. (2011) Outline of the 2011 off the pacific coast of Tohoku earthquake (Mw 9.0) seismicity: foreshocks, mainshock, aftershocks, and induced activity. *Earth Planets Space* 63: 513–518. DOI: 10.5047/eps.2011.05.019

Hong JK and Uang CM (2012) Cyclic testing of a metal building moment frame system with web-tapered members. *Journal of Constructional Steel Research* 70: 248–255. DOI: 10.1016/j.jcsr.2011.09.005

Huang Y, Wu JP, Zhang TZ, et al. (2008) Relocation of the M8.0 Wenchuan earthquake and its aftershock sequence. *Science in China Series D-Earth Sciences* 51(12): 1703–1711. DOI: 10.1007/s11430-008-0135-z

Jeon JS (2013) Aftershock Vulnerability Assessment of Damaged Reinforced Concrete Buildings in California. Ph.D. thesis, School of Civil and Environmental Engineering, Georgia Institute of Technology, Atlanta, USA.

Jeon JS, DesRoches R, Lowes LN, et al. (2015b) Framework of aftershock fragility assessment–case studies: older California reinforced concrete building frames. *Earthquake*

Engineering & Structural Dynamics 44(15): 2617–2636. DOI: 10.1002/eqe.2599

Jeon JS, Park JH and DesRoches R (2015a) Seismic fragility of lightly reinforced concrete frames with masonry infills. *Earthquake Engineering and Structural Dynamics* 44(11): 1783–1803. DOI: 10.1002/eqe.2555

Khansefid A (2021a) An investigation of the structural nonlinearity effects on the building seismic risk assessment under mainshock–aftershock sequences in Tehran metro city. *Advances in Structural Engineering* 24(16): 3778–3791. DOI: 10.1177/13694332211038446

Khansefid A (2021b) Lifetime risk-based seismic performance assessment of buildings equipped with supplemental damping and base isolation systems under probable mainshock-aftershock scenarios. *Structures* 34: 3647–3666. DOI: 10.1016/j.istruc.2021.09.093

Li Y, Song R and Lindt JW (2014) Collapse fragility of steel structures subjected to earthquake mainshock-aftershock sequences. *Journal of Structural Engineering* 140(12): 1–10. DOI: 10.1061/(ASCE)ST.1943-541X.0001019

Malekizadeh M (2017) Investigating the Vertical Component Effects of Earthquake on the Seismic Performance of Wide-Span Steel Gabled Structures Located on Flexible Substrate Using Incremental Dynamic Analysis. MSc thesis, Department of Civil Engineering, Academic Center for Education, Culture and Research, Khuzestan Branch, Ahvaz, Iran.

Malekizadeh M and Pirasteh AA (2021a) Designing steel gabled structures by ASD and LRFD methods and proposing formulas for estimating base shear and total weight. In: *5th International Conference on Civil, Architecture and Urban Management*. Tbilisi, Georgia.

Malekizadeh M, Fanaie N and Pirasteh AA (2021b) Probabilistic seismic assessment of steel gabled frames with web-tapered members under near-fault ground motions along strike-normal and strike-parallel components. *Structures* 34: 4142–4157. DOI: 10.1016/j.istruc.2021.10.007

Malekizadeh M, Fanaie N and Pirasteh AA (2022a) Vertical component effects of earthquake and soil-structure interaction on steel gabled frames. *Journal of Constructional Steel Research* 196: 107409. DOI: 10.1016/j.jcsr.2022.107409

Malekizadeh M, Fanaie N and Pirasteh AA (2022b) Seismic reliability evaluation of steel gabled frames consisting of web-tapered members using joint analysis of hazard and fragility. *Structures* 37: 459–468. DOI: 10.1016/j.istruc.2022.01.004

Malekizadeh M, Pirasteh AA and Siahpolo N (2018) Evaluating the effect of earthquake vertical component on large bay steel gabled frame located on flexible substrate using IDA. *Journal of Structural and Construction Engineering* 6(3): 18–37. DOI: 10.22065/jsce.2018.94460.1283

MBMA (2012) *Metal Building Systems Manual*. Cleveland, OH, USA: Metal Building Manufacturers Association.

Michele M, Stefano RD, Chiaraluce L, et al. (2016) The Amatrice 2016 seismic sequence: a preliminary look at the mainshock and aftershocks distribution. *Annals of Geophysics* 59(5): 7227. DOI: 10.4401/ag-7227

Moustafa A and Takewaki L (2016) Modeling critical ground-motion sequences for inelastic structures. *Advances in Structural Engineering* 13(4): 665–679. DOI: 10.1260/1369-4332.13.4.665

Nazari N, Lindt JW and Li Y (2015) Effect of mainshock-aftershock sequences on woodframe building damage fragilities. *Journal of Performance of Constructed Facilities* 29: 04014036. DOI: 10.1061/(ASCE)CF.1943-5509.0000512

Nehrp (2000) Recommended Provisions for Seismic Regulations for New Buildings. Washington DC, USA: Building Seismic Safety Council.

Newman A (2004) Metal Building Systems: Design and Specifications. NY, USA: McGraw-Hill.

OpenSees (2018) Open system for earthquake engineering simulation. *Pacific Earthquake Engineering Research Center*. Berkeley, CA, USA: University of California.

PEER-NGA Database (2006) Pacific Earthquake Engineering Research Center. Berkeley, CA, USA: University of California. https://peer.berkeley.edu/nga/

Priestley MJN (1993) Myths and fallacies in earthquake engineering-conflicts between design and reality. *Bulletin of the New Zealand Society for Earthquake Engineering* 26(3): 329–341. DOI: 10.5459/bnzsee.26.3.329-341

Raghunandan M, Liel AB and Luco N (2015) Aftershock collapse vulnerability assessment of reinforced concrete frame structures. *Earthquake Engineering & Structural Dynamics* 44(3): 419–439. DOI: 10.1002/eqe.2478

Ribeiro FL, Barbosa AR and Neves LC (2014) Application of reliability-based robustness assessment of steel moment resisting frame structures under post-mainshock cascading events. *Journal of Structural Engineering* 140(8): 1–12. DOI: 10.1061/(ASCE)ST.1943-541X.0000939

Rinaldin G, Amadio C and Fragiacomo M (2017) Effects of seismic sequences on structures with hysteretic or damped dissipative behaviour. *Soil Dynamics and Earthquake Engineering* 97: 205–215. DOI: 10.1016/j.soildyn.2017.03.023

Ruiz-García J and Aguilar JD (2015) Aftershock seismic assessment taking into account post-mainshock residual drifts. *Earthquake Engineering & Structural Dynamics* 44(9): 1391–1407. DOI: 10.1002/eqe.2523

Ruiz-García J and Miranda E (2006a) Residual displacement ratios for assessment of existing structures. *Earthquake Engineering & Structural Dynamics* 35(3): 315–336. DOI: 10.1002/eqe.523

Ruiz-García J and Miranda E (2006b) Evaluation of residual drift demands in regular multi-story frames for performance-based seismic assessment. *Earthquake Engineering & Structural Dynamics* 35(13): 1609–1629. DOI: 10.1002/eqe.593

Ruiz-García J and Miranda E (2010) Probabilistic estimation of residual drift demands for seismic assessment of multi-story framed buildings. *Engineering Structures* 32(1): 11–20. DOI: 10.1016/j.engstruct.2009.08.010

Shi F, Saygili G, Ozbulut OE, et al. (2020) Risk-based mainshock-aftershock performance assessment of SMA braced steel frames. *Engineering Structures* 212: 110506. DOI: 10.1016/j.engstruct.2020.110506

Shome N and Cornell CA (1999) *Probabilistic Seismic Demand Analysis of Nonlinear Structures*. Report No. RMS-35. CA, USA: Stanford University.

Silwal B and Ozbulut OE (2018) Aftershock fragility assessment of steel moment frames with self-centering Dampers. *Engineering Structures* 168: 12–22. DOI: 10.1016/j.engstruct.2018.04.071

Song R, Li Y and Lindt JW (2014) Impact of earthquake ground motion characteristics on collapse risk of post-mainshock buildings considering aftershocks. *Engineering Structures* 81: 349–361. DOI: 10.1016/j.engstruct.2014.09.047

Song R, Li Y and Lindt JW (2013) Consideration of mainshock-aftershock sequences into performance-based seismic engineering. *Proceedings of the Structures Congress*. USA: American Society of Civil Engineers. DOI: 10.1061/9780784412848.189

Su M, Wang H, Wang Z, et al. (2017) Shaking table tests on steel portal frames consisting of non-compact tapered members. *Journal of Constructional Steel Research* 128: 473–482. DOI: 10.1016/j.jcsr.2016.09.009

Trevlopoulos K, Guéguen P, Helmstetter A, et al. (2020) Earthquake risk in reinforced concrete buildings during aftershock sequences based on period elongation and operational earthquake forecasting. *Structural Safety* 84: 101922. DOI: 10.1016/j.strusafe.2020.101922

Uma SR, Pampanin S and Christopoulos C (2010) Development of probabilistic framework for performance-based seismic assessment of structures considering residual deformations. *Journal of Earthquake Engineering* 14(7): 1092–1111. DOI: 10.1080/13632460903556509

Vamvatsikos D and Cornell CA (2002) Incremental dynamic analysis. *Earthquake Engineering & Structural Dynamics* 31(3): 491–514. DOI: 10.1002/eqe.141

Wang D, Wu C, Zhang Y, et al. (2019) Elastic-plastic behavior of AP1000 nuclear island structure under mainshock-aftershock sequences. *Annals of Nuclear Energy* 123: 1–17. DOI: 10.1016/j.anucene.2018.09.015

Wang G, Wang Y, Lu W, et al. (2017) Damage demand assessment of mainshock-damaged concrete gravity dams subjected to aftershocks. *Soil Dynamics and Earthquake Engineering* 98: 141–154. DOI: 10.1016/j.soildyn.2017.03.034

Wang ZS, Su MZ, Li QC, et al. (2012) Pseudo-static experimental study of a single-story single-bay light-weight portal frame with tapered members. *China Civil Engineering Journal* 45(7): 24–30. (in Chinese).

Yakhchalian M, Nicknam A and Ghodrati Amiri G (2015) Optimal vector-valued intensity measure for seismic collapse assessment of structures. *Earthquake Engineering and Engineering Vibration* 14(1): 37–54. DOI: 10.1007/s11803-015-0005-6

Zhai CH, Zheng Z, Li S, et al. (2017) Damage accumulation of a base-isolated RCC building under mainshock-aftershock seismic sequences. *KSCE Journal of Civil Engineering* 21(1): 364–377. DOI: 10.1007/s12205-016-0701-4

Zhang S, Wang G and Sa W (2013) Damage evaluation of concrete gravity dams under mainshock-aftershock seismic sequences. *Soil Dynamics and Earthquake Engineering* 50: 16–27. DOI: 10.1016/j.soildyn.2013.02.021

Zhang YN, Zhi XD and Fan F (2020) Influence of multiple earthquakes on single-layer reticulated dome and its shaking-table test. *International Journal of Steel Structures* 20: 101–120. DOI: 10.1007/s13296-019-00272-w